

Feasibility and Applications of the Spin-Echo Modulation Option for a Small Angle Neutron Scattering Instrument at the European Spallation Source [☆]

A. Kusmin, W. G. Bouwman, A. A. van Well, C. Pappas

Department of Radiation Science and Technology, Faculty of Applied Sciences, Delft University of Technology, 2629JB Delft, The Netherlands

Abstract

We describe theoretical and practical aspects of spin-echo modulated small-angle neutron scattering (SEMSANS) as well as the potential combination with SANS. Based on the preliminary technical designs of SKADI (a SANS instrument proposed for the European Spallation Source) and a SEMSANS add-on, we assess the practicability, feasibility and scientific merit of a combined SANS and SEMSANS setup by calculating tentative SANS and SEMSANS results for soft matter, geology and advanced material samples that have been previously studied by scattering methods. We conclude that lengths from 1 nm up to 0.01 mm can be observed simultaneously in a single measurement. Thus, the combination of SANS and SEMSANS instrument is suited for the simultaneous observation of a wide range of length scales, e.g. for time-resolved studies of kinetic processes in complex multiscale systems.

Keywords: SANS, SESANS, SEMSANS

1. Introduction

The range of length scales typically observed in a small-angle neutron scattering (SANS) experiment is between 1 nm and several 100 nm. Larger length scales on the μm range can be observed either with ultra SANS (USANS) [1] or with spin-echo small-angle neutron scattering (SESANS) [2]. Recently, a new technique to measure SESANS using the modulation of neutron spin-echo polarization across the incident beam has been suggested and tested [3–7]. As the components required to perform the modulation are located before the sample and do not affect the configuration of the SANS instrument, the idea of a combined spin-echo modulation small angle neutron scattering (SEMSANS) and a SANS instrument has been put forward [8].

An implementation of this idea was proposed for SKADI, one of the SANS instruments to be built at ESS, and has been included in the list of potential add-ons for this instrument [9]. Preliminary requirements and potential designs of the SEMSANS add-on have been discussed in the technical reports [10, 11]. In this paper, we take a detailed look into the technical feasibility of combined SANS and SEMSANS measurements and the potential applications.

We start by a short description of the SEMSANS technique, and the relation between the SANS and SEMSANS results. After that, based on the technical designs of SKADI and of a SEMSANS add-on, we calculate the boundaries of length scale regions accessible by SANS and SEMSANS and show that they overlap. We discuss the impact of the SEMSANS add-on on SANS measurements, and calculate SEMSANS signals for soft matter, geological, advanced material samples that have already been studied by neutron scattering. The results of the calculations show that

[☆]© 2017. This manuscript version is made available under the CC-BY-NC-ND 4.0 license <http://creativecommons.org/licenses/by-nc-nd/4.0/>

the combination of SANS with SEMSANS is feasible and can cover a wide range of length scales simultaneously, which makes it useful for kinetic process studies in complex, multiscale samples in time resolved mode.

2. A SEMSANS experiment

2.1. The technique

A simplified scheme of the SANS instrument together with a SEMSANS add-on is shown in Fig. 1. The neutron beam is polarised in the Y direction. The first pair of V-coils [12] acts as a $\pi/2$ -flipper: it adiabatically rotates the polarisation into the XZ plane thus triggering Larmor precessions. The central pair of V-coils performs a π -flip, and the last pair stops the precessions by performing a $\pi/2$ -flip. The net precession angle is the difference between the precession angles ϕ_1 and ϕ_2 accumulated before and after the π -flip, respectively. The spin echo (se) polarization measured after transmission through an analyser is defined as: $P_{se} = P_0 \cos(\phi_1 - \phi_2)$, where P_0 is the beam polarization in the absence of Larmor precessions, typically the product of the polarizer and analyzer efficiencies, and $\phi_i = \gamma B_i t_i$, where γ is neutron gyromagnetic ratio, and t_i is the time-of-flight of the neutron beam through the i th triangular region¹.

Let us first assume that all neutron trajectories are parallel to Z axis. The middle of the first triangular region is at $x = 0$, the path through this region is $l_1(x) = \frac{H-2x}{\tan \theta_0}$, where H is the height of the triangle. The middle of the second triangular region is shifted towards negative x by Δ , the path through this region is $l_2(x) = \frac{H-2(x+\Delta)}{\tan \theta_0}$.

Using $t_i(x) = l_i(x)m\lambda/h$, where h is Planck constant, m and λ are neutron's mass and wavelength, and Larmor

constant, $c = m\gamma/h$, we arrive at:

$$\phi_1 = [c\lambda B_1 H / \tan \theta_0] - [2c\lambda B_1 x / \tan \theta_0] \quad (1a)$$

$$\phi_2 = [c\lambda B_2 (H - 2\Delta) / \tan \theta_0] - [2c\lambda B_2 x / \tan \theta_0] \quad (1b)$$

The shift Δ is fixed at

$$\Delta = H(1 - B_1/B_2)/2 \quad (2)$$

to make $\phi_1 - \phi_2 = 0$ at $x = 0$, that is, to realize spin-echo in the center of the detector.

From eqs. 1a-1b the spin echo polarization is

$$P_{se}(x) = P_0 \cos(2\pi x/\zeta) \quad (3)$$

where the oscillation period, ζ , is given by:

$$\zeta = \frac{\pi \tan \theta_0}{c\lambda(B_2 - B_1)} \quad (4)$$

The resulting neutron intensities for the eigenstates $|+\rangle$ and $|-\rangle$ are:

$$I_{se}^{\pm}(x) = \frac{I(x)[1 \pm P_{se}(x)]}{2} \quad (5)$$

So far we neglected the dependence of the net precession angle on the divergence in the XZ plane. For a divergent beam, when the distances between the detector, and the centers of the first and the second triangular regions, L_1 and L_2 , respectively, satisfy the condition [3]:

$$B_1 L_1 = B_2 L_2 \quad (6)$$

measured intensities can be described by a modified version of eq. 5:

$$I_{se}^{\pm}(x) = \frac{I(x)[1 \pm V(x) \cos(2\pi x/\zeta)]}{2} \quad (7)$$

where $V(x)$ is the so-called visibility.

In the absence of a sample, the visibility is $V_0(x)$:

$$V_0(x) = P_0 R_{pixel} R_{\Delta\lambda}(x) \quad (8)$$

where $R_{\Delta\lambda}(x)$ accounts for the effect of wavelength resolution (see Appendix A), and R_{pixel} accounts for a finite spatial resolution of the detector (see Appendix B).

¹For brevity, the contribution of the i th guide field to ϕ_i is omitted. This is justified because the guide fields are tuned in such a way that their contribution to the net precession angle is zero.

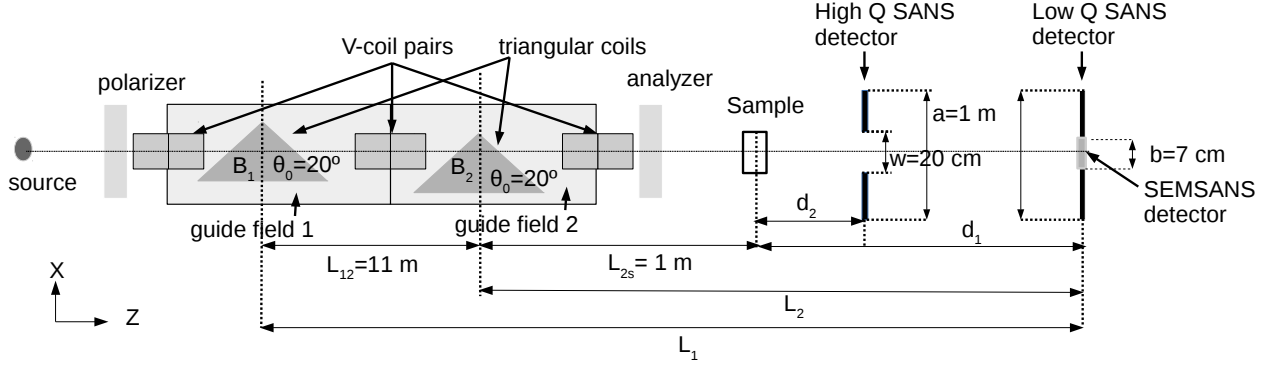


Figure 1: A sketch of a SANS+SEMSANS instrument (view from above, not to scale). The magnetic fields B_1 and B_2 , and guide fields 1 and 2 are parallel to Y axis and point into one direction. The first and the last V-coil pairs act as $\pi/2$ -flippers, the middle pair acts as a π -flipper. Both SANS detectors are squares $a \times a$; the high Q SANS detector has a square window in the center, $w \times w$. The beam stop is a square, $b \times b$. The size of the SEMSANS detector is limited by the beam stop size. The distance d_2 is fixed at $0.2 \times d_1$, d_1 can be set to 8 m or 20 m. The angle $\theta_0 = 20^\circ$ corresponds to triangular coils tested in Delft [6].

In the presence of a sample, the x -coordinate of the pixel where a neutron will be detected depends on whether it is scattered or not and, if it is scattered, on the scattering angle. Thus, the visibility of modulations will be reduced to an extent that depends on the intensity and angular dependence of the small-angle scattering, more details are given in the next section. The normalized visibility, $V_s = V(x)/V_0(x)$, thus reflects the scattering from the sample only, because the normalization cancels all additional effects due to the finite wavelength resolution and spatial detector resolution.

Please note that the shift of the second triangular precession region relative to the first one, i.e. Δ from eq. 2, is independent of magnetic field settings because of the condition expressed by eq. 6. The use of such a shift is a new approach. Alternatively, instead of triangular coils, magnets with an inclined foil flipper can also be used [8].

2.2. Relation between SEMSANS, SESANS, and SANS

It was shown in Ref. [13] that the normalized visibility, V_s , is the equivalent of the normalized neutron spin-echo polarization measured by SESANS. Therefore, it can be described by the same theory [14] leading to:

$$V_s(\delta_{SE}) = \exp[\Sigma_{exp} t (G_{exp}(\delta_{SE}) - 1)] \quad (9)$$

where t is the sample thickness, and the subscript exp reflects the dependence of respective parameters on experimental conditions (such as detector size, sample-detector distance etc). In SEMSANS the spin-echo length is given by the relation:

$$\delta_{SE} = \lambda d_1 / \zeta = \frac{c(B_2 - B_1)d_1 \lambda^2}{\pi \tan \theta_0} \quad (10)$$

where d_1 is the distance between sample and detector.

For small scattering angles² Σ_{exp} is related to the differential coherent SANS cross-section $\frac{d\Sigma(\mathbf{Q})}{d\Omega}$, through:

$$\Sigma_{exp} = \frac{\lambda^2}{(2\pi)^2} \int_{pixel} \frac{d\Sigma(\mathbf{Q})}{d\Omega} dQ_x dQ_y \quad (11)$$

The meaning of Σ_{exp} can be best seen for the case of a thin sample, in which case the product $\Sigma_{exp} t$ is just the fraction of neutrons that are scattered into the solid angle covered by the pixel of the SEMSANS detector.

The function $G_{exp}(\delta_{SE})$ in eq. 9 is the experimentally observed projection of the autocorrelation function of the scattering length density, $\gamma(\mathbf{r})$ [15]. Its theoretical definition, $G_{tot}(\delta_{SE})$, can be expressed as the Hankel transform of $d\Sigma(\mathbf{Q})/d\Omega$ if the scattering is isotropic [15]:

$$G_{tot}(\delta_{SE}) = \frac{1}{2\pi\xi_{tot}} \int_0^\infty J_0(Q\delta_{SE}) \frac{d\Sigma(Q)}{d\Omega} Q dQ \quad (12)$$

²That is, when $\tan \theta \approx \theta$, and $Q_z \approx 0$. This condition is fulfilled for SEMSANS.

where J_0 is the zeroth-order Bessel function of the first kind, and the subscript *tot* (for "total") indicates that the upper integration limit is infinity. The correlation length, ξ_{tot} , is given by [15]:

$$\xi_{tot} = \frac{1}{2\pi} \int_0^\infty \frac{d\Sigma(Q)}{d\Omega} Q dQ \quad (13)$$

The experimentally determined $V_s(\delta_{SE})$ can be analyzed using eq. 9 where the functions Σ_{exp} and $G_{exp}(\delta_{SE})$ can be related to $d\Sigma(Q)/d\Omega$ through:

$$\xi_{exp} = \frac{\Sigma_{exp}}{\lambda^2} = \frac{1}{2\pi} \int_0^{Q_{SEMSANS}^{max}} \frac{d\Sigma(Q)}{d\Omega} Q dQ \quad (14)$$

$$G_{exp}(\delta_{SE}) = \frac{1}{2\pi\xi_{exp}} \int_0^{Q_{SEMSANS}^{max}} J_0(Q\delta_{SE}) \frac{d\Sigma(Q)}{d\Omega} Q dQ \quad (15)$$

The obvious difference between eqs. 12, 13 and eqs. 14, 15 is in the integration range, which in the latter case is limited by acceptance angles to the maximum accessible Q , $Q_{SEMSANS}^{max}$.

A detailed account for an effect of acceptance angles on measured SEMSANS intensities and on $V_s(\delta_{SE})$ has been given in Appendix C. In case when $Q_{SEMSANS}^{max}$ is particularly low, that is, when a significant part of small-angle scattering cross-section is not registered by the SEMSANS detector, eq. 9 no longer holds and a more general result, eq. C.24 in Appendix C, should be used.

3. Practical aspects of combining SANS and SEMSANS

In order to assess the impact of the SEMSANS add-on on a SANS instrument, it is important to estimate the accessible Q - and δ_{SE} -ranges and identify a possible overlap. This was performed by fixing the major instrument parameters, for SANS according to the technical design of SKADI [9], and for SEMSANS according to previous reports [10, 11].

3.1. Q -range accessible to SANS

In the high flux mode SKADI uses every neutron pulse leading to a bandwidth of 5.5 Å and 7.2 Å for a sample-

detector distance of $d_1=20$ m and $d_1=8$ m, respectively. In the wide Q mode every second pulse is used leading to a doubling of the bandwidth. For the combination with SEMSANS, the incident neutron beam must be polarized; therefore, based on the current SKADI design, the minimum wavelength λ^{min} cannot be lower than 3 Å [9].

The minimum Q for SANS is given by:

$$Q_{SANS}^{min} = \frac{4\pi}{\lambda^{max}} \sin(\text{atan}(\frac{0.5\sqrt{2}b}{d_1})/2) \approx \frac{\sqrt{2}\pi b}{d_1\lambda^{max}} \quad (16)$$

where b is the size of the beam stop. Since $d_2 = 0.2 d_1$, the maximum Q accessible by SANS is:

$$Q_{SANS}^{max} = \frac{4\pi}{\lambda^{min}} \sin(\text{atan}(\frac{0.5\sqrt{2}a}{0.2d_1})/2) \approx \frac{5\sqrt{2}\pi a}{d_1\lambda^{min}} \quad (17)$$

where a is the size of the SANS detector.

3.2. δ_{SE} -range accessible to SEMSANS

The spin-echo length range can be calculated from eq. 10 and eq. 6. Since the measurements can be done at more than one sample-to-detector distances (d_1) and, therefore, at different L_1 and L_2 distances, it is preferable to make the d_1 -dependence explicit and rewrite these equations as follows:

$$\delta_{SE} = \frac{d_1 L_{12} c B_1 \lambda^2}{(d_1 + L_{2s}) \pi \tan \theta_0} \quad (18)$$

$$B_2 = B_1 \frac{L_{12} + L_2}{L_2} = B_1 \frac{L_{12} + L_{2s} + d_1}{L_{2s} + d_1} \quad (19)$$

where L_{2s} and L_{12} are as defined in Fig. 1.

The following parameters are fixed: $\theta_0 = 20^\circ$, $L_{2s}=1$ m, and $L_{12} = 11$ m. The other two parameters, d_1 and λ , depend on the configuration of the host SANS instrument. Once the latter is fixed, the δ_{SE} range can only be modified by changing B_1 . The magnetic field limits of the triangular coils are $B_1^{min} = 0.1$ mT and $B_2^{max} = 15$ mT. The limiting δ_{SE} values are δ_{SEB}^{min} (calculated from λ^{min} and B_1^{min}), and δ_{SEB}^{max} (calculated from λ^{max} and B_1^{max} , which, in turn, is calculated from B_2^{max} and eq. 19).

Due to the finite detector spatial resolution the visibility of the sample and empty beam measurements is reduced by a factor R_{pixel} , which depends on the pixel size

Table 1: SKADI instrument configurations and the limits on the accessible Q and spin-echo length (δ_{SE}) ranges. For calculation details see Sec. 3. $\delta_{SE_B}^{min}$ and $\delta_{SE_B}^{max}$ are the limits due to minimum and maximum magnetic fields, respectively. $\delta_{SE_{pixel}}^{max}$ is the limit due to the spatial resolution of the SEMSANS detector.

Configuration			SANS range		SEMSANS range		
Mode	d_1 [m]	$\lambda^{min}; \lambda^{max}$ [Å]	$Q_{SANS}^{min}; Q_{SANS}^{max}$ [Å ⁻¹]	$\frac{2\pi}{Q_{SANS}^{min}}$ [μm]	$\delta_{SE_B}^{min}$ [μm]	$\delta_{SE_B}^{max}$ [μm]	$\delta_{SE_{pixel}}^{max}$ [μm]
High flux	20	3; 8.5	$1.8 \times 10^{-3}; 0.37$	0.34	0.038	30	126
Wide Q	20	3; 14	$1.1 \times 10^{-3}; 0.37$	0.57	0.038	82	207
High flux	8	3; 10.2	$3.8 \times 10^{-3}; 0.87$	0.16	0.036	28	60
Wide Q	8	3; 17.4	$2.2 \times 10^{-3}; 0.87$	0.28	0.036	81	103

and oscillation period ζ (see Appendix B). The minimum acceptable R_{pixel} is set to 0.75 and the corresponding limit on the maximum spin-echo length, $\delta_{SE_{pixel}}^{max}$, is calculated from eq. B.3 using λ^{max} and a pixel size of 55 μm, a spatial resolution which is already reached by state-of-the-art detectors [16].

As can be seen from Tab. 1, the minimum and maximum spin-echo lengths are related to the magnetic field limits, leading to the range of $[\delta_{SE_B}^{min}; \delta_{SE_B}^{max}]$. This range must be distinguished from the range covered in a single measurement with an arbitrary B_1 , which is $[\delta_{SE}(B_1, \lambda_{min}); \delta_{SE}(B_1, \lambda_{max})]$.

The comparison of the maximum lengths observable with SANS ($2\pi/Q_{SANS}^{min}$) and the minimum lengths observable with SEMSANS ($\delta_{SE_B}^{min}$) reveals a substantial overlap between the length scales accessible to SANS and SEMSANS, for all instrument configurations.

3.3. The effect of acceptance angles

As it can be seen from eq. 15, the correlation function $G_{exp}(\delta_{SE})$ is a Fourier transform over an experimentally accessible Q -region limited by

$$Q_{SEMSANS}^{max} \approx \frac{2\pi\theta_{SEMSANS}^{max}}{\lambda} \quad (20)$$

where $\theta_{SEMSANS}^{max}$ is the maximum accepted scattering angle. The $\theta_{SEMSANS}$ -limits are given by (see Appendix D):

$$\theta_{SEMSANS} \in \left(\frac{x}{d_1} \pm \left(\frac{S}{d_1} + \frac{S_C + S}{d_C} \right) \right) \quad (21)$$

where x is the X -coordinate of the SEMSANS detector pixel, the sizes of sample and collimation apertures along X axis are $2S$, and $2S_C$, respectively, and the distance between the two apertures is d_C .

For $d_1 = 8$ m, $d_C = 8$ m, $S_C = 1.5$ cm, and $S = 0.5$ cm (aperture sizes correspond to Fig. 7 in Ref. [9]) and for $x = 0$, $|\theta_{SEMSANS}| < 3.125$ mrad. With increasing x , the range of accepted angles becomes increasingly asymmetric around zero. For example, at $x = 1$ mm, $-3 < \theta_{SEMSANS} < 3.25$ mrad, at $x = 1.5$ cm, $-1.25 < \theta_{SEMSANS} < 5$ mrad. This asymmetry decreases at larger d_1 -distances.

Because of an x -dependence of the accepted $\theta_{SEMSANS}$ -range, the function $G_{exp}(\delta_{SE})$ and normalized visibility $V_s(\delta_{SE})$ may be x -dependent as well (cf. eq. 15 and eq. 9). In general, a fit of a SANS model to $V_s(\delta_{SE})$ can account for this x -dependence. However, for simplicity, such an x -dependence can also be removed. To do that, only the intensity measured in a narrow central region of the SEMSANS detector around $x = 0$, e.g. $|x| < 2$ mm should be used to calculate $V_s(\delta_{SE})$. In this paper, we choose the latter option and calculate $Q_{SEMSANS}^{max}$, $G_{exp}(\delta_{SE})$, and $V_s(\delta_{SE})$ for $x = 0$.

Finally, please note that to increase counting statistics, $V_s(\delta_{SE})$ can be calculated from measured intensities that are summed up along the Y -axis of the SEMSANS detector. In such a case, however, the range of accepted scatter-

ing angles in YZ plane will be broader than in XZ plane. This can be taken into account by using a modified version of eqs. 14,15, where a single integral over $|Q|$ is replaced by a double integral over Q_x and Q_y . More details are given in Appendices C and D. Calculations in this paper were done under assumption that $Q^{max} = Q_x^{max} = Q_y^{max}$.

3.4. Interference of the SEMSANS add-on with the SANS measurements

As can be seen in Fig. 1, all SEMSANS components with the exception of the detector are located before the sample. Thus, they do not interfere with the scattered beam. Their impact consists in an attenuation of the incident beam and possibly a modification of the collimation by the polarizer, V-coils, triangular coils, and the analyzer.

The major impact of a polarizer and an analyzer on SANS measurements consists in a reduction of the incident beam intensity by at least factor $2 \times 2 = 4$. If a ^3He cell is used as analyzer the divergence of the incident beam is not affected but the intensity losses will be higher.

The scattering from the coils is mainly due to refraction, which is significant for cylindrical wires [17]. Therefore, the parts of the coils exposed to the beam should use flat, smooth and thin wires to minimize refraction, absorption and scattering. The neutron beam passes through six wire planes of the six V-coils at 90° angle and four wire planes of two triangular coils at 20° angle. For a thickness of a planar wire of 0.5 mm the total wire thickness becomes $6 \times 0.5 + 4 \times 0.5 / \sin(20^\circ) \approx 9$ mm. For aluminium wires, this corresponds to a transmission of 98% at $\lambda = 3$ Å, and 93% at $\lambda = 10$ Å.

Behind the sample, a state-of-the-art MCP detector may be used, such as described in ref. [16]. The dimensions of its active surface are 3 cm by 3 cm and are smaller than dimensions of a beam stop (7 cm by 7 cm), but its actual size is larger. This size will probably be reduced in the future. Alternatively, the MCP detector can be placed behind the high Q SANS detector if the latter has a win-

dow in the center.

In addition, as the pixel size of the SANS detector is expected to be 3 mm by 3 mm, intensity oscillations with a period of a few mm could be observed with SANS as well. Their amplitude can be estimated from eq. 8 by calculating the factor $R_{pixel}R_{\Delta\lambda}(x)$ using eqs. B.2 and A.8 for the borders of the beam stop, i.e. $x = \pm b/2$. For $\zeta = 16$ mm (the largest period in the results shown later), $R_{\Delta\lambda}(x = b/2, d\lambda/\lambda = 0.04) \approx 0.97$, and $R_{pixel}(p=3\text{mm}) = 0.94$. Thus, the amplitude of intensity oscillations is almost the same as in the SEMSANS detector. On the other hand, in the case of a smaller period of 1.6 mm, the oscillations will not be observed by SANS because of $R_{\Delta\lambda}(x = b/2, d\lambda/\lambda = 0.04) \approx 0.06$, and $R_{pixel}(p=3\text{mm}) = 0.06$.

The effect of oscillations on the measured SANS cross-sections can be removed by taking the shim or the average of the intensities (cf. eq. 7). In any case no oscillations will be observed with the high Q SANS detector because the condition in eq. 6 will never be fulfilled.

3.5. Practical aspects with respect to the analysis of SANS and SEMSANS measurements

A substantial difference in the combined SANS-SEMSANS data analysis arises from multiple scattering effects, which affect differently the measured patterns. In SANS, where multiple scattering is a major issue, two extreme cases can be considered.

In the case of multiple small-angle scattering, the probability to be scattered at a small angle is much higher than at larger angles. As a result, the shape of a measured SANS curve is affected, however, procedures such as described in Ref. [18] allow to correct for this and to obtain accurate structural information.

In the second case, multiple scattering is primarily caused by the high probability to be scattered at angles larger than the angles accepted by a SANS detector, e.g. due to a substantial incoherent scattering cross-section. In this case, multiple scattering does not change the Q -dependence

of the measured SANS cross-section, but it leads to a scattering background, which, however, can be corrected using empirical procedures [19].

In the following we will focus on multiple SANS effects, as they are the most frequent. Their impact can be evaluated by calculating the SANS transmission, $T_{SANS}(\lambda)$, from eq. E.3. This impact is substantial for $T_{SANS}(\lambda)$ lower than 80% (see Appendix E for more details).

In SEMSANS, multiple scattering is taken into account by eq. 9, however, it becomes a severe limitation when it leads to $V_s(\delta_{SE})$ close to zero. In such a case multiple scattering limits the maximum usable spin-echo length, which becomes lower than δ_{SE}^{max} -limits given in Tab. 1. To prevent this, we define a constraint, $T_{SEMSANS} > 0.01$, where

$$T_{SEMSANS} = \exp(-\Sigma_{exp}t) \quad (22)$$

and Σ_{exp} is given by eq. 14. For $0 < G(\delta_{SE}) < 1$ it follows from eq. 9 and eq. 22 that $T_{SEMSANS} < V_s(\delta_{SE}) < 1$.

For an accurate test of scattering models against experimental SEMSANS data using eq. 9, we estimate that $V_s(\delta_{SE})$ should be lower than 0.99, which is somewhat arbitrary but based on experience with SESANS experiments. Qualitatively, it can also be justified as follows: for a relative error of 1% the deviation of $V_s(\delta_{SE})$ from unity becomes significant only for $V_s(\delta_{SE})$ less or equal to 0.99.

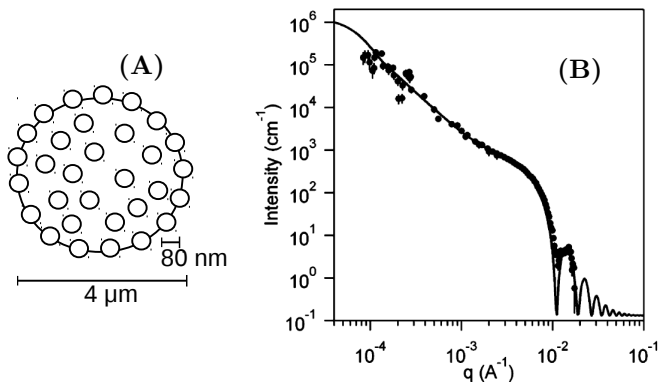


Figure 2: A: Sketch of a raspberry particle. B: Measured and calculated differential SANS+USANS cross-sections; adapted with permission from ref. [20]; copyright (2012) American Chemical Society.

3.6. Calculation of SEMSANS signal and sample transmission

As mentioned above several samples have been considered and for every one, we first calculated $d\Sigma(Q)/d\Omega$ using the model and parameters from the original publication (see the supplementary material for details). Then we selected one of the four SKADI configurations and the corresponding minimum wavelength, λ^{min} . As a result, the total wavelength range was fixed to $(\lambda^{min}, \lambda^{max})$, and the Q -range accessible with SANS was fixed as well. The maximum δ_{SE} , δ_{SE}^{max} , was chosen based on the maximum (anticipated) size of structural features in the sample. Using eq. 18 and λ^{max} , we calculated B_1 and the entire δ_{SE} -range. Then, the following calculations were done in the specified order:

1. $\xi_{tot}(\delta_{SE})$ from eq. 13;
2. $G_{tot}(\delta_{SE})$ from eq. 12;
3. the acceptance angle $\theta_{SEMSANS}^{max}$ from eq. 21 calculated for the center of SEMSANS detector, i.e. for $x = 0$;
4. $Q_{SEMSANS}^{max}(\delta_{SE})$ from eqs. 20;
5. $\xi_{exp}(\delta_{SE})$ from eq. 14;
6. $G_{exp}(\delta_{SE})$ from eq. 15;
7. $V_s(\delta_{SE})$ from eq. C.24 (via eq. C.21, eq. C.22 and eq. C.23, see Appendix C for details);
8. $T_{SANS}(\delta_{SE})$ from eq. E.3 and $T_{SEMSANS}(\delta_{SE})$ from eq. 22.

4. Examples of applications

4.1. Raspberry particles

We first consider the example of raspberry particles which are present e.g. in Pickering emulsions consisting of two immiscible phases, typically oil and water. Small solid particles located at the oil-water interfaces form an elastic "shell" that prevents coalescence. Raspberry particles formed by adsorption of polystyrene latex particles on polydisperse oil droplets, schematically shown in Fig.

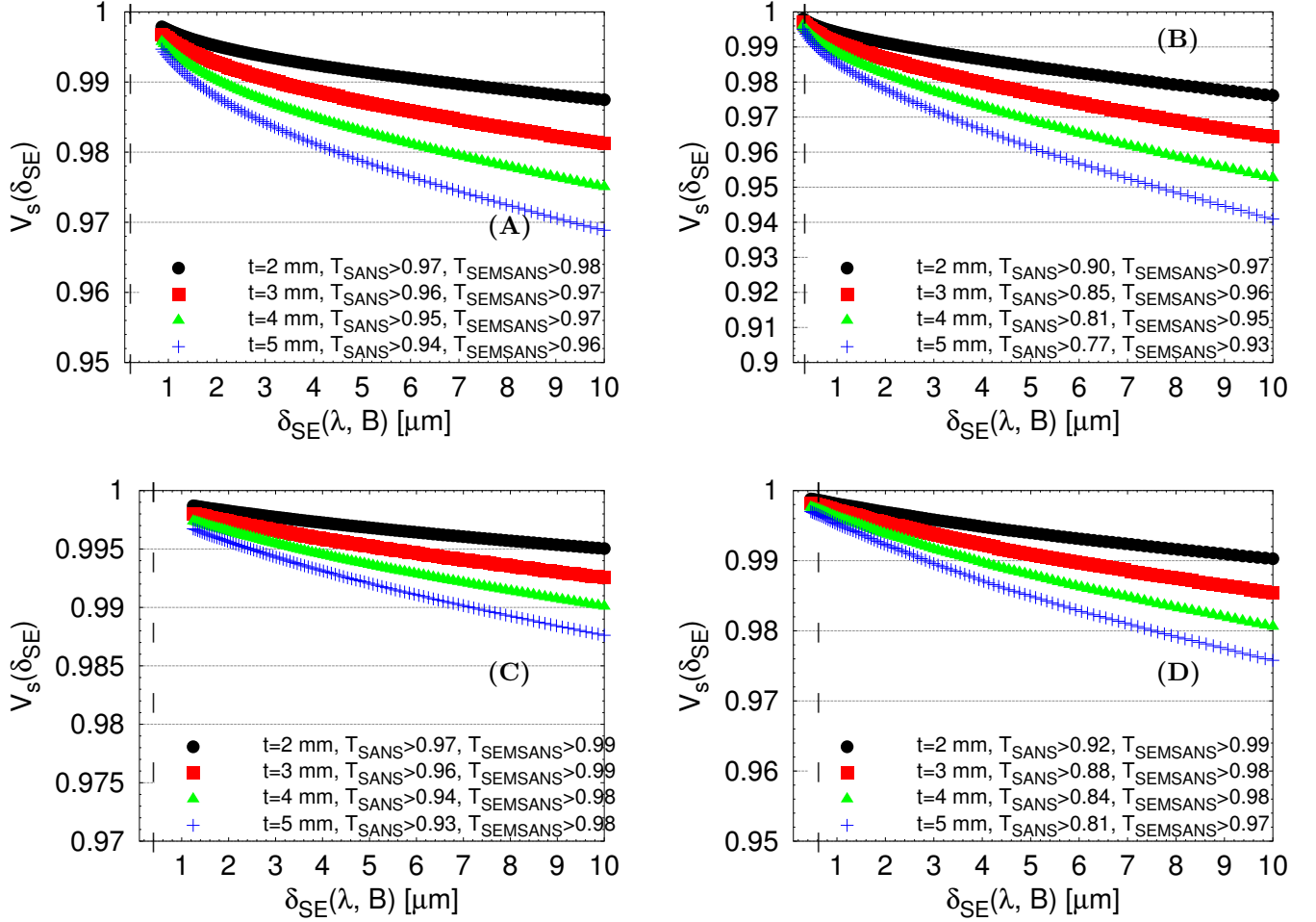


Figure 3: $V_s(\delta_{SE})$ for raspberry particles, at several thicknesses (t), $\lambda_{min} = 3 \text{ \AA}$. A: high flux mode, $d_1=8 \text{ m}$, $\lambda_{max} = 10.2 \text{ \AA}$, $B_1=2.4 \text{ mT}$, $\zeta^{max} = 2.8 \text{ mm}$; B: wide Q mode, $d_1=8 \text{ m}$, $\lambda_{max} = 17.4 \text{ \AA}$, $B_1=0.8 \text{ mT}$, $\zeta^{max} = 8 \text{ mm}$; C: high flux mode, $d_1=20 \text{ m}$, $\lambda_{max} = 8.5 \text{ \AA}$, $B_1=3.3 \text{ mT}$, $\zeta^{max} = 5 \text{ mm}$; D: wide Q mode, $d_1=20 \text{ m}$, $\lambda_{max} = 14 \text{ \AA}$, $B_1=1.2 \text{ mT}$, $\zeta^{max} = 13 \text{ mm}$. A dashed vertical line corresponds to $\delta_{SE} = 2\pi/Q_{SANS}^{min}$, that is, the maximum length probed by SANS.

2Å, have been measured with SANS (down to Q of 10^{-3} \AA^{-1}) and USANS (down to Q of $8 \times 10^{-5} \text{ \AA}^{-1}$) in a combined study [20]. Maximum observable distances correspond to 0.63 \mu m and 7.8 \mu m , for SANS and USANS, respectively. The example of experimental and fitted $d\Sigma(Q)/d\Omega$ is shown in Fig. 2B.

The SEMSANS results for the maximum spin-echo length of 10 \mu m and several sample thicknesses are shown in Fig. 3. First of all, the overlap between SANS and SEMSANS is only achieved in the wide Q mode of SKADI (Fig. 3B,D), because in this case the δ_{SE} -region is broader due to the broader λ -range. Second, measurements at a longer

sample-detector distance (d_1) lead to a lower $V_s(\delta_{SE})$ and are better suited for a more accurate SEMSANS modeling (compare Fig. 3B vs. Fig. 3D). The lower $V(\delta_{SE})$ values can be explained as follows: for larger d_1 , $Q_{SEMSANS}^{max}$ gets smaller, so does Σ_{exp} (cf. eq. 14), and, as a consequence, $V_s(\delta_{SE})$ approaches unity (cf. eq. 9).

Finally, the results for different sample thicknesses in Fig. 3B show that for larger thicknesses $V_s(\delta_{SE})$ becomes lower, thus more appropriate for SEMSANS measurement. However, at the same time T_{SANS} decreases, which implies higher multiple scattering effects on the SANS signal. In all cases $T_{SEMSANS} > 0.9$, the multiple scattering impact

on SEMSANS is negligible.

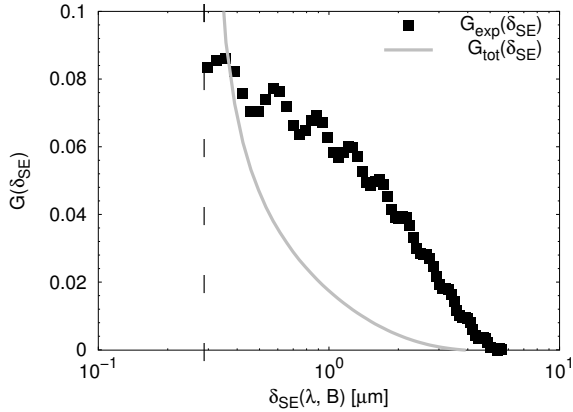


Figure 4: $G(\delta_{SE})$ for raspberry particles calculated from $d\Sigma(Q)/d\Omega$ via eq. 15 ($G_{exp}(\delta_{SE})$) and eq. 12 ($G_{tot}(\delta_{SE})$) for the wide Q mode and $\lambda_{min} = 3 \text{ \AA}$ at $d_1 = 8 \text{ m}$ (the same conditions as in Fig. 3B). A dashed vertical line corresponds to $\delta_{SE} = 2\pi/Q_{SE}^{min}$.

Fig. 4 depicts the correlation functions $G_{exp}(\delta_{SE})$ and $G_{tot}(\delta_{SE})$ thus illustrating the effect of the finite upper integration limit in eq. 15, $Q_{SEMSANS}^{max}(\delta_{SE})$ due to the finite acceptance angle of the SEMSANS detector. $G(\delta_{SE})$ (cf. eq. 12) is a real space correlation function [15]. Thus, the experimentally obtained $G_{exp}(\delta_{SE})$ is directly related to the structure of the sample. For example, in Fig. 4, $G_{exp}(\delta_{SE})$ becomes zero for δ_{SE} , which exceeds the maximum correlation length of the structure. Therefore, the latter can be estimated from the intercept of $G_{exp}(\delta_{SE})$ with the δ_{SE} -axis. In fact this correlation length is larger than the average diameter of a raspberry particle due to the effect of polydispersity. Note that the noticeable difference between $G_{exp}(\delta_{SE})$ and $G_{tot}(\delta_{SE})$ renders a visual analysis of $G_{exp}(\delta_{SE})$ less reliable and in some cases even impossible. However, a proper, detailed analysis of $G_{exp}(\delta_{SE})$ includes fitting of a Hankel transform of a structural model in terms of $d\Sigma(Q)/d\Omega$, and this calculation does include the finite acceptance angle effect.

4.2. Fuel, rocks and minerals

SANS, USANS or their combination are commonly used for structural characterizations over a wide range of length

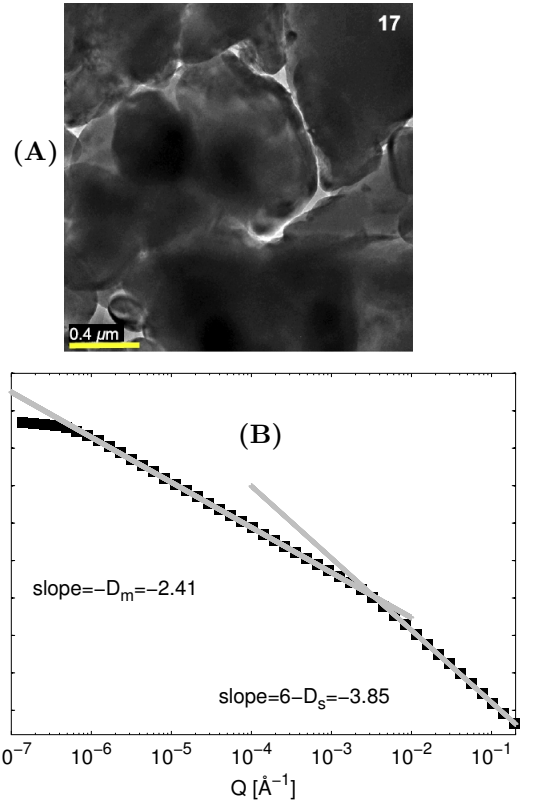


Figure 5: A: a TEM image of chalk; reprinted with permission from ref. [21], copyright (2013) Elsevier. B: $d\Sigma(Q)/d\Omega$ of a chalk sample calculated using the results from a combined SANS, USANS and electron imaging study [21].

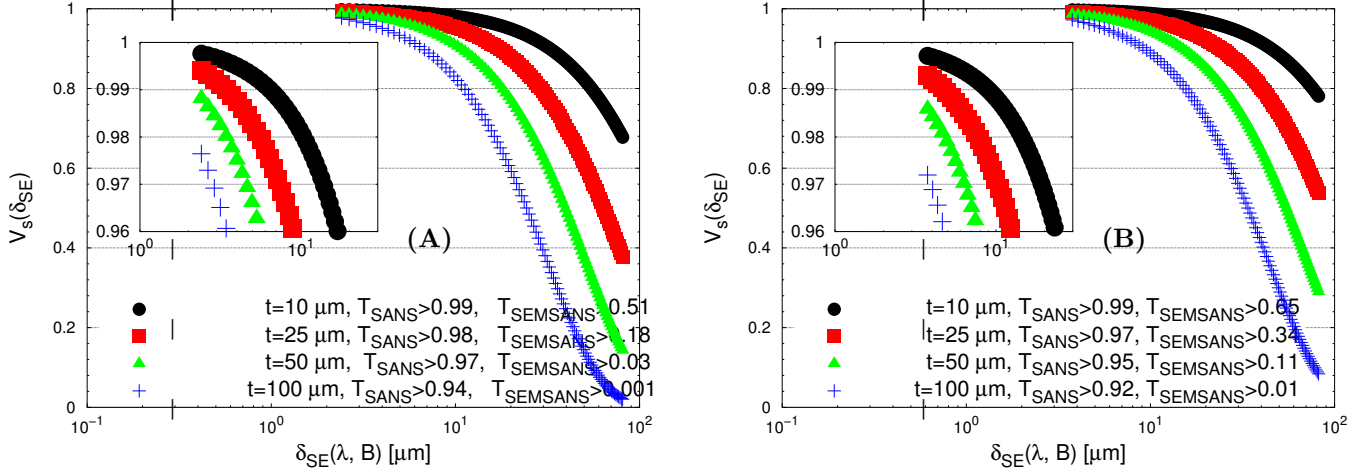


Figure 6: $V_s(\delta_{SE})$ for a chalk sample of several thicknesses (t), wide Q mode, $\lambda_{min} = 3 \text{ \AA}$. A: $d_1=8 \text{ m}$, $\lambda_{max} = 17.4 \text{ \AA}$, $B_1=6.7 \text{ mT}$, $\zeta^{max} = 1 \text{ mm}$; B: $d_1=20 \text{ m}$, $\lambda_{max} = 14 \text{ \AA}$, $B_1=9.8 \text{ mT}$, $\zeta^{max} = 1.6 \text{ mm}$. Inset figures show that for the two thickest samples the condition $V_s(\delta_{SE}) < 0.99$ is met.

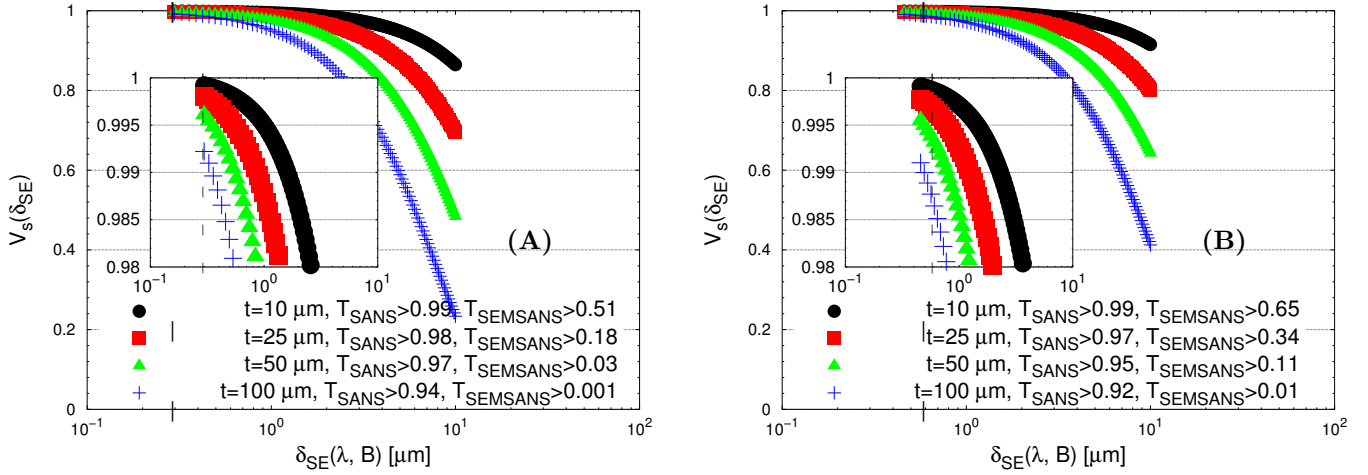


Figure 7: $V_s(\delta_{SE})$ for a chalk sample of several thicknesses (t), wide Q mode, $\lambda_{min} = 3 \text{ \AA}$, and for lower magnetic field settings than in Fig. 6. A: $d_1=8 \text{ m}$, $\lambda_{max} = 17.4 \text{ \AA}$, $B_1=2.4 \text{ mT}$, $\zeta^{max} = 8 \text{ mm}$; B: $d_1=20 \text{ m}$, $\lambda_{max} = 14 \text{ \AA}$, $B_1=3.2 \text{ mT}$, $\zeta^{max} = 13 \text{ mm}$. Inset figures show that the condition $V_s(\delta_{SE}) < 0.99$ is met only for the thickest sample in subfigure B and only for $\delta_{SE} > 2\pi/Q_{SANS}^{min}$.

scales in geology, mineralogy or hydrocarbon recovery. Examples of such studies are provided in diagenesis (change of a sedimentary rock into a different rock) [21, 22], pore structure in coals [23] and in nuclear graphite [24], hydrocarbon generation [25], tight gas reservoirs [26] or gas shales [27]. These results are often complemented by other studies, which extend the structural information over length scales larger than $1 \mu\text{m}$, like neutron imaging [24] or transmission electron microscopy (TEM), such as the image of chalk in Fig. 5A.

The differential cross-section of chalk calculated from

the parameters obtained from SANS, USANS and imaging is given in Fig. 5B. The slope of the curve in the Q -region covered by USANS and imaging gives information on the mass fractal dimension of the pore network (D_m). The slope of the curve in the region of larger Q -values (the region covered by SANS) gives the surface fractal dimension D_s of individual pores.

The original USANS experiment on chalk [21] was performed with an incident wavelength of $\lambda = 2.38 \text{ \AA}$ and on a 0.15 mm thick sample in order to reduce multiple scattering effects. For longer wavelengths such as those

considered in this comparative study, the samples should be much thinner.

The $V_s(\delta_{SE})$ calculated for the chalk sample and for a maximum δ_{SE} of 100 μm is shown in Fig. 6. In this case, as it is important to cover a broad δ_{SE} -range, only the wide Q mode is considered. In addition the δ_{SE}^{max} in a real experiment may not reach 100 μm because of limitations on the maximum magnetic field. In this configuration, a broad range of length scales is covered but the δ_{SE} -range has no overlap with the region accessed by SANS. In order to achieve an overlap between SANS and SEMSANS, the SEMSANS measurements should be performed at a smaller magnetic field, such as in Fig. 7, where, however, δ_{SE} does not exceed ≈ 10 μm . Thus, the technical constraints do not allow to reach an overlap between SANS and SEMSANS and at the same time a maximum δ_{SE} of 100 μm .

Another limitation occurs from multiple scattering effects. As $T_{SANS} > 0.90$, multiple scattering does not significantly influence the SANS results. On the other hand, it does limit the SEMSANS measurement because the $T_{SEMSANS}$ -values decrease to zero at spin echo lengths shorter than δ_{SE}^{max} for the largest sample thicknesses. A compromise between SANS and SEMSANS along the lines of Subsec. 3.5 leads to a maximum sample thickness of ≈ 50 μm , which, in some cases, can not be easily achieved without modifying the mesoscopic structure of the sample. An interesting aspect of the small-angle scattering though is that it probes the structure in the direction perpendicular to the incident beam, and thus SEMSANS can probe the structure even on the length scales larger than the sample thickness.

Calculated $G_{exp}(\delta_{SE})$ and $G_{tot}(\delta_{SE})$ are shown in Fig. 8. The difference between the two is rather small in contrast to the raspberry particle case given in Fig. 4. This small difference is due to the fact that the differential SANS cross-section of chalk decreases rapidly with increasing Q and thus the cut-off at the high Q region does not

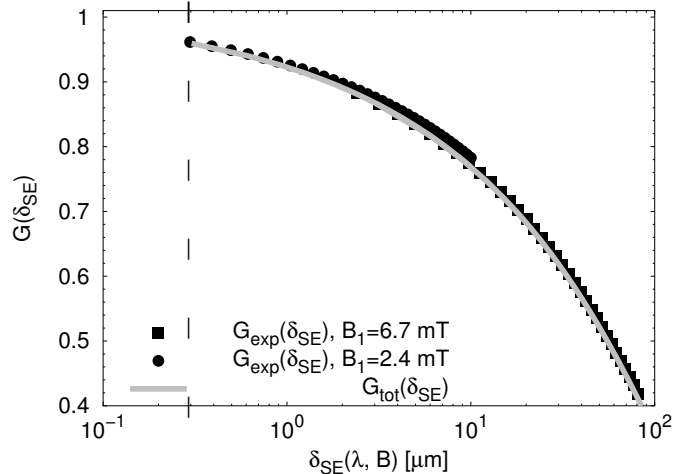


Figure 8: $G_{exp}(\delta_{SE})$ and $G_{tot}(\delta_{SE})$ for chalk sample, for the wide Q mode, $d_1=8$ m, and $\lambda_{min} = 3$ \AA (the total wavelength range is $3 \text{\AA} < \lambda < 17.4 \text{\AA}$).

significantly alter the result of Hankel transform.

4.3. Growth of monodisperse spherical particles

Monodisperse colloidal particles with sizes up to $\approx 1\text{-}2$ μm have numerous applications [28]. The growth of such particles or kinetic processes involving their functionalization are potential science cases for a combined SANS and SEMSANS instrument. An example of such particles are "Stöber particles", which are monodisperse spherical silica particles prepared by the method described in 1968 by Stöber et al. [29].

A number of SAXS and USAXS experiments have been performed on Stöber particles with diameters in the range from 10 to 100 nm, depending on reaction times and conditions [31, 32]. Stöber particles prepared by a multistage method may have much larger diameters, larger than 1 μm [33]. Transmission electron microscopy shows that such Stöber particles are not homogeneous but contain a series of thin (≈ 15 nm thick) concentric spherical shells of larger density [30] as schematically shown in Fig. 9A.

USAXS experiments on Stöber particles were performed with Q larger than $\approx 2 \times 10^{-3}$ \AA^{-1} , which corresponds to a maximum observable length of ≈ 300 nm. Longer length scales (up to 500 nm) have been studied recently with

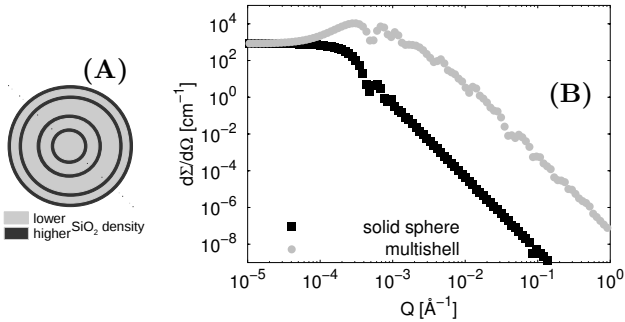


Figure 9: A: A model of a SiO₂ particle based on TEM images of large (diameter of $\approx 1.8 \mu\text{m}$) Stöber particles prepared by a multi-stage method [30]. B: $d\Sigma(Q)/d\Omega$ for $d\lambda/\lambda = 18\%$ and in an aqueous solution ($\text{H}_2\text{O}:\text{D}_2\text{O} \approx 1:1$), for two models of Stöber particles: solid spheres with a radius of $\approx 1 \mu\text{m}$, and multishell spheres (spheres of the same size and average density, but with nine concentric shells which have a higher density than the density between the shells).

SESANS [34]. Time-resolved combined SANS and SEM-SANS experiments would allow to cover a wide range of length scales and observe in-situ the growing Stöber particle as a function of reaction time. This will provide important input to understand how particles with tailored properties can be produced and at the same time discriminate between various models of their inner structure.

We have modeled Stöber particles prepared by a multi-stage method as homogeneous solid spheres with a radius of $\approx 1 \mu\text{m}$ and as spheres of the same radius and the same average density but with several thin concentric shells with increased density. Sphere radii and the concentric shells were taken from an earlier study [30] and details are given in the supplement.

The resulting differential SANS cross-sections are shown in Fig. 9B for an aqueous solution ($\text{H}_2\text{O}:\text{D}_2\text{O} \approx 1:1$). Approximate matching of the solvent scattering length density (SLD) to the average SLD of a multishell particle (the contrast is just $\approx 5 \times 10^7 \text{ cm}^{-2}$) allows to distinguish between two different models of internal structure.

Fig. 10 provides examples of the calculated $V_s(\delta_{SE})$ for the case where a broad wavelength range is used and $d_1 = 8 \text{ m}$. A larger d_1 -distance would decrease the acceptance angle and lead to $V_s(\delta_{SE})$ values that are too close

to unity, similarly to the raspberry particles case. Also, if λ_{min} increases, the minimum δ_{SE} increases, and the overlap between SANS and SEMSANS shrinks.

For all sample thicknesses and for both wavelength ranges, T_{SANS} and $T_{SEMSANS}$ are always higher than 90 %, indicating that multiple scattering is negligible for both SANS and SEMSANS. The deduced minimum total sample transmission (determined from eq. E.1) for $t = 4 \text{ mm}$ is 30 % at $\lambda^{min} = 3 \text{ \AA}$ (when $\lambda^{max} = 17.4 \text{ \AA}$) and 24% at $\lambda^{min} = 6 \text{ \AA}$ (when $\lambda^{max} = 20.4 \text{ \AA}$).

An example of $G_{exp}(\delta_{SE})$ and $G_{tot}(\delta_{SE})$ is shown in Fig. 11. It can be seen that the solid spheres $G(\delta_{SE})$ differs from that of multishell spheres. Thus, it is possible to distinguish between the two models using SEMSANS. In addition, $G_{tot}(\delta_{SE})$ and $G_{exp}(\delta_{SE})$ are close to each other for solid spheres but are quite different for multishell spheres. This reflects the fact that for multishells, the ratio between the differential scattering cross-section at large Q and small Q is larger than for solid spheres. Therefore, the cut-off of the high Q region via an upper integration limit in eq. 15 has a larger effect on $G_{exp}(\delta_{SE})$ for multishell than for solid spheres.

5. Discussion

5.1. Potential applications

The three examples presented above represent three different science cases illustrating potential scientific applications for a combined SANS and SEMSANS instrument. In the case represented by the raspberry particles, the macroscopic incoherent scattering cross-section is low, and the scattering by large particles is significant but not very strong. It is thus possible to combine SANS and SEMSANS to cover a wide range of length scales in a single measurement. In the case of a strong SANS scatterer like chalk, which scatters across a large range of length scales, it is not possible to cover the wide range of interest in a single measurement without a gap, which however, amounts to just a few micrometers out of the total

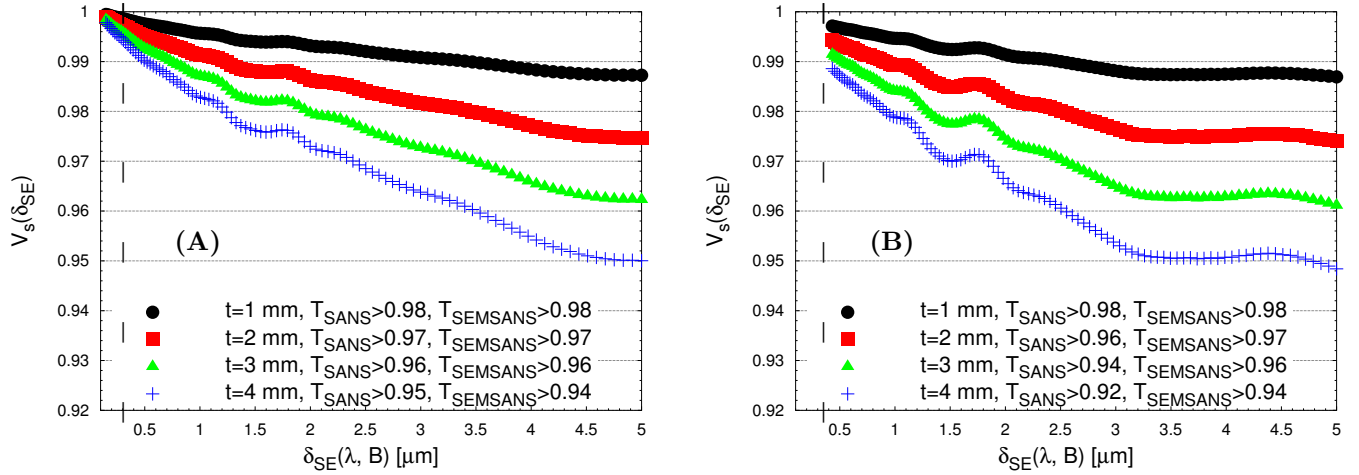


Figure 10: Experimental $V_s(\delta_{SE})$ for a sample of Stöber particles modeled by multishell spheres of several thicknesses (t), for wide Q mode and $d_1=8$ m. A: $\lambda_{min}=3$ Å, $\lambda_{max}=17.4$ Å, $B_1=0.4$ mT, $\zeta^{max}=16$ mm; B: $\lambda_{min}=6$ Å, $\lambda_{max}=20.4$ Å, $B_1=0.3$ mT, $\zeta^{max}=11$ mm. A dashed vertical line corresponds to $\delta_{SE} = 2\pi/Q_{SANS}^{min}$.

range of about four orders of magnitude, from 1 nm to 80 μ m. In the last case represented by an aqueous solution of Stöber particles, the macroscopic incoherent scattering cross-section is large but the coherent scattering contribution at small Q is relatively weak. Here, too, a wide range of length scales can be covered in a single measurement but the total transmission may be as low as 30 % although with negligible multiple SANS contribution. For all three cases a sample thickness can be found that keeps the impact of multiple scattering at an acceptable level and at the same time leads to reasonable SEMSANS signals, $V_{SE} \leq 0.99$.

The specific parameters of the SEMSANS add-on considered here lead to a range of length scales covered without a gap between the regions accessed by SANS and SEMSANS extending up to ≈ 10 μ m. A larger range can be covered but with a gap or by performing SEMSANS measurements with more than one magnetic field setting, but what are the implications?

The magnetic field settings do not interfere with the SANS measurements as long as both "spin-up" and "spin-down" intensities are recorded for every magnetic field. Therefore, with respect to SANS, the use of more than one magnetic field has just one small disadvantage: the SANS measurement time is reduced by the time required

to change magnetic field, which is a few seconds. For SEMSANS, the choice of several magnetic fields settings will only affect the time resolution (for kinetic studies), which can be pondered by the potential benefit of covering a much broader length range.

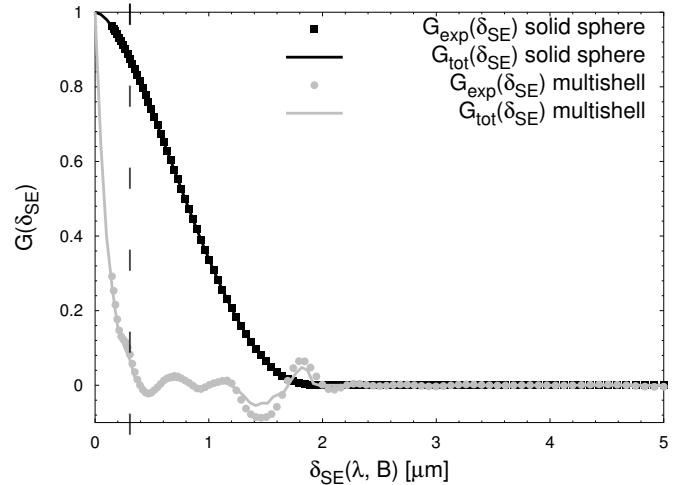


Figure 11: $G_{exp}(\delta_{SE})$ and $G_{tot}(\delta_{SE})$ for Stöber particles modeled by solid and multishell spheres, for $\lambda_{min} = 3$ Å, and other conditions corresponding to Fig. 10A. The peaks in $G(\delta_{SE})$ correspond to diameters of the shells with increased densities (outer shell radii are given in the supplementary material).

5.2. Feasibility

SANS is a well-established technique, and the feasibility of SEMSANS experiments has also been proven [3–7]. Hence, the combination of SANS with SEMSANS depends on the specific scientific question and required measurement times.

Section 3.4 showed that the primary effect of a SEMSANS add-on on a SANS instrument consists in the reduction of incident beam intensity by a factor between 5 and 10, depending on the performance of the polariser and analyser in front of the sample. Furthermore, in order to make sure that the measured SANS cross-sections are not affected by the intensity modulation, the SANS intensities must be adequately averaged to obtain the shim intensity, which may decrease the time resolution as well, typically by a factor of two. Indeed, the maximum oscillation periods provided for all application examples, and the estimation of the reduction in the oscillation amplitude given in Sec. 3.4, indicate that such an averaging will be required in many cases. Thus the question is: what is the time resolution that can be achieved for kinetic SANS measurements with adequate counting statistics? In general, for time-resolved measurements the time resolutions of SANS and SEMSANS do not need to match each other. Time binning can be done so as to ensure that counting statistics is acceptable for both SANS and SEMSANS. Such an adaptive binning is especially easy in the case when data acquisition is done in the "event mode".

The examples of applications show that sample thicknesses suitable for combined SANS and SEMSANS measurements are similar to those that would be chosen for a stand-alone SANS measurement, thus keeping multiple scattering effects to an adequate level. Consequently, the SEMSANS add-on would reduce the time resolution by a factor $10 \times 2 = 20$ with respect to a stand-alone SANS measurement. This is of course a severe drawback, which however may be compensated by the high flux of the ESS. The incident neutron beams at the ESS are expected to

be at least 10 times more intense than in other sources, which would render combined SANS and SEMSANS time resolved measurements an attractive option. These would be at least as good as SANS measurements nowadays, but with an additional structural information provided by SEMSANS.

Tentative measurement times and time resolutions for SEMSANS measurements can be estimated by considering that a large part of intensity measured by the SEMSANS detector comes from the transmitted neutron beam. Therefore, even if only a narrow part in the center of MCP detector is used (e.g. for $|x| < 1$ mm, in order to have a symmetric range of accepted scattering angles for all x , see eq. 21), the counting statistics should not be a problem. In addition, the high brilliance of the incident beam at ESS will not pose a problem for the SEMSANS detector. High counting rates reaching 10^8 cm⁻²s⁻¹ can be handled by state-of-the-art MCP detectors, with at the same time a spatial resolution of 55 μ m [16].

5.3. An effect of finite acceptance angles

The examples above show that for the raspberry particles and multishell Stöber particles $G_{exp}(\delta_{SE})$ is quite different from $G_{tot}(\delta_{SE})$, while for rocks and large solid Stöber particles the difference between the two is negligible. This difference is caused by the finite acceptance angle of the SEMSANS detector. In the cases where the differential scattering cross-section is a fast decaying function of Q (e.g. for fractal structures), the cut-off at Q -values larger than $Q_{SEMSANS}^{max}$ has a negligible effect on the Hankel transform.

However, as in general the structure of a sample is unknown, it is impossible to predict the effect of acceptance angle. In this case a visual analysis of $G_{exp}(\delta_{SE})$ may lead to incorrect conclusions and requires the fit of a SANS model on $G_{exp}(\delta_{SE})$ using eqs. 14-15 by taking into account the acceptance angle and the corresponding $Q_{SEMSANS}^{max}$. This is analogous to the angular and wave-

length resolution effects in SANS, which affect the positions of peaks or minima but can be taken into account during the fit.

5.4. The choice of experimental parameters

The major application for combining SANS and SEM-SANS in a single measurements are time-resolved studies of kinetic processes and multiscale phenomena covering a large region of length scales. These are the cases where the substantial decrease in intensity caused by the SEMSANS add-on can be justified.

On the other hand, the largest range of spin-echo lengths and the best $V(\delta_{SE})$ -signal can be achieved for just one configuration of SKADI, namely for a sample to detector distance of 8 m in the wide Q mode. Because the neutron flux decreases dramatically for longer wavelengths, such a combined setup should use a minimum wavelength achievable for a polarised neutron beam (for SKADI, it is $\lambda_{min} = 3 \text{ \AA}$). This minimum wavelength would also maximise the overlap between the SEMSANS and SANS length scales. In such a case the choice of magnetic field depends on the maximum δ_{SE} that should be reached.

Thus, the only remaining free parameter is the sample thickness, the choice of which will affect the multiple SANS effect on the measured differential SANS cross-sections, and possibly, on the maximum spin-echo length that can be observed with SEMSANS. The sample thickness will also affect the SANS counting statistics data and the quality of the SEMSANS data (that is, to what extent $V(\delta_{SE})$ differs from 1). However, multiple scattering depends on the structure of each specific sample and there is no simple recipe on how to select an optimal sample thickness. This must be estimated using sample transmission, SEMSANS signal, and counting statistics obtained by test measurements or by calculations.

5.5. Simultaneous analysis of SANS+SEMSANS results

A simultaneous analysis of the SANS and SEMSANS data requires the transformation of either 1) $G_{exp}(\delta_{SE})$ to

$d\Sigma(Q)/d\Omega$; or 2) $d\Sigma(Q)/d\Omega$ to $G_{exp}(\delta_{SE})$. Another option is to simultaneously refine a SANS model against original SANS and SEMSANS data sets.

The first two options require a numerical Hankel transformation of experimental data. The result of this transform is sensitive to the minimum and maximum Q -(or δ_{SE})-values, to corrections for multiple scattering and incoherent scattering background, and to the value of sample transmission (which is difficult to measure in the presence of strong forward scattering).

The third option can be realized as a simultaneous refinement of a model against SANS data sets and the Hankel transform of the same model against SEMSANS data sets. The implementation of the key component of this option, namely, fitting of the Hankel transform of a SANS model to $V_s(\delta_{SE})$ measured in SEMSANS is being implemented at Delft University of Technology in collaboration with developers of the SASview program [35].

Please note that in the presence of very strong small-angle scattering, for example, from large particles and strong scattering contrast, the scattering may no longer be adequately modeled by single-particle scattering models that are based on the first Born approximation[36]. However, judging by the calculated T_{SANS} and $T_{SEMSANS}$ -values, this should not be the case for all examples discussed above.

Summary

Based on the technical design of the SANS instrument SKADI, which will be built at ESS, and on preliminary characteristics of a SEMSANS add-on we have shown that a wide range of length scales over 4 orders of magnitude, from $\approx 1 \text{ nm}$ to $\approx 10 \text{ }\mu\text{m}$, can be covered simultaneously in a single measurement by combining the two techniques. The calculations involved several combinations of instrument parameters and wavelength ranges. The performance was discussed by considering specific examples from soft matter, geoscience, and advanced materials samples that

were previously studied with SANS, USANS and imaging. The results show that for all samples adequate quality of SANS and SEMSANS measurements can be obtained by choosing suitable parameters, such as the sample thickness. Thus, a SEMSANS add-on on a SANS instrument such as SKADI can be used to simultaneously observe a wide range of length scales and for time-resolved studies of kinetic processes in complex multiscale samples.

Acknowledgments

This work was financially supported by Delft University of Technology and The Netherlands Organization for Scientific Research (NWO) through the OYSTER project as a contribution to the pre-construction phase of the European Spallation Source. The authors thank J. Plomp as well as the ESS and SKADI teams for valuable discussions.

References

References

- [1] J. G. Barker, C. J. Glinka, J. J. Moyer, M. H. Kim, A. R. Drews, M. Agamalian, *J. Appl. Crystallogr.* 38 (2005) 1004–1011.
- [2] M. T. Rekveldt, J. Plomp, W. G. Bouwman, W. H. Kraan, S. Grigoriev, M. Blaauw, *Rev. Sci. Instrum.* 76 (2005).
- [3] W. G. Bouwman, C. P. Duif, R. Gaehler, *Physica B* 404 (2009) 2585–2589.
- [4] M. Strobl, A. S. Tremsin, A. Hilger, F. Wieder, N. Kardjilov, I. Manke, W. G. Bouwman, J. Plomp, *J. Appl. Phys.* 112 (2012).
- [5] M. Strobl, F. Wieder, C. P. Duif, A. Hilger, N. Kardjilov, I. Manke, W. G. Bouwman, *Physica B* 407 (2012) 4132–4135.
- [6] M. Sales, J. Plomp, K. Habicht, M. Strobl, *J. Appl. Crystallogr.* 48 (2015) 92–96.
- [7] M. Strobl, M. Sales, J. Plomp, W. G. Bouwman, A. S. Tremsin, A. Kaestner, C. Pappas, K. Habicht, *Sci. Rep.* 5 (2015) 16576.
- [8] W. G. Bouwman, C. P. Duif, J. Plomp, A. Wiedenmann, R. Gaehler, *Physica B* 406 (2011) 2357–2360.
- [9] S. Jaksch, D. Martin-Rodriguez, A. Ostermann, J. Jestin, S. Duarte Pinto, W. G. Bouwman, J. Uher, R. Engels, H. Frielinghaus, *Nucl. Instrum. Methods Phys. Res. Sect. A.* 762 (2014) 22–30.
- [10] S. Duarte Pinto, W. G. Bouwman, J. Plomp, C. Pappas, Requirements and limitations for a combined SANS-SESANS Instrument at the ESS (DWP 1.1.1), Technical Report, 2014.
- [11] S. Duarte Pinto, J. Plomp, W. G. Bouwman, C. Pappas, Conclusion on what type of Larmor labeling method is the best option for the ESS (DWP 1.1.2), Technical Report, 2014.
- [12] W. H. Kraan, M. T. Rekveldt, P. T. Por, *Nucl. Instrum. Methods Phys. Res. Sect. A.* 300 (1991) 35–42.
- [13] M. Strobl, *Sci. Rep.* 4 (2014) 7243.
- [14] M. T. Rekveldt, W. G. Bouwman, W. H. Kraan, O. Uca, S. V. Grigoriev, K. Habicht, T. Keller, in: F. Mezei, C. Pappas, T. Gutberlet (Eds.), *Neutron Spin Echo Spectroscopy: Basics, Trends and Applications*, Lecture Notes in Physics, 601 ed., 2003, pp. 87–99.
- [15] R. Andersson, L. F. van Heijkamp, I. M. de Schepper, W. G. Bouwman, *J. Appl. Crystallogr.* 41 (2008) 868–885.
- [16] A. S. Tremsin, J. B. McPhate, J. V. Vallergera, O. H. W. Siegmund, W. B. Feller, E. Lehmann, A. Kaestner, P. Boillat, T. Panzner, U. Filges, *Nucl. Instrum. Meth. A.* 688 (2012) 32–40.
- [17] J. Plomp, J. G. Barker, V. O. de Haan, W. G. Bouwman, A. A. van Well, *Nucl. Instrum. Methods Phys. Res. Sect. A.* 574 (2007) 324–329.
- [18] J. Schelten, W. Schmatz, *J. Appl. Crystallogr.* 13 (1980) 385–390.
- [19] M. Shibayama, T. Matsunaga, M. Nagao, *J. Appl. Crystallogr.* 42 (2009) 621–628.
- [20] K. Larson-Smith, A. Jackson, D. C. Pozzo, *Langmuir* 28 (2012) 2493–2501.
- [21] H.-W. Wang, L. M. Anovitz, A. Burg, D. R. Cole, L. F. Allard, A. J. Jackson, A. G. Stack, G. Rother, *Geochim. Cosmochim. Acta* 121 (2013) 339–362.
- [22] L. M. Anovitz, D. R. Cole, G. Rother, L. F. Allard, A. J. Jackson, K. C. Littrell, *Geochim. Cosmochim. Acta* 102 (2013) 280–305.
- [23] A. P. Radlinski, M. Mastalerz, A. L. Hinde, A. Hainbuchner, H. Rauch, M. Baron, J. S. Lin, L. Fan, P. Thiyagarajan, *Int. J. Coal. Geol.* 59 (2004) 245–271.
- [24] Z. Zhou, W. G. Bouwman, H. Schut, S. Desert, J. Jestin, S. Hartmann, C. Pappas, *Carbon* 96 (2016) 541–547.
- [25] A. P. Radlinski, C. J. Boreham, P. Lindner, O. Randl, G. D. Wignall, A. Hinde, J. M. Hope, *Org. Geochem.* 31 (2000) 1–14.
- [26] C. R. Clarkson, M. Freeman, L. He, M. Agamalian, Y. B. Melnichenko, M. Mastalerz, R. M. Bustin, A. P. Radlinski, T. P. Blach, *Fuel* 95 (2012) 371–385.
- [27] H. E. King, Jr., A. P. R. Eberle, C. C. Walters, C. E. Kliever, D. Ertas, C. Huynh, *Energy Fuels* 29 (2015) 1375–1390.
- [28] Y. N. Xia, B. Gates, Y. D. Yin, Y. Lu, *Adv. Mater.* 12 (2000) 693–713.
- [29] W. Stober, A. Fink, E. Bohn, *J. Colloid Interface Sci.* 26 (1968) 62–&.

- [30] V. M. Masalov, E. A. Kudrenko, N. A. Grigoryeva, K. V. Ezdakova, V. V. Roddatis, N. S. Sukhinina, M. V. Arefev, A. A. Mistonov, S. V. Grigoriev, G. A. Emelchenko, *Nano* 8 (2013) 1350036.
- [31] H. Boukari, G. G. Long, M. T. Harris, *J. Colloid Interface Sci.* 229 (2000) 129–139.
- [32] A. Gutsche, A. Daikeler, X. Guo, N. Dingenouts, H. Nirschl, *J. Nanopart. Res.* 16 (2014).
- [33] V. M. Masalov, N. S. Sukhinina, E. A. Kudrenko, G. A. Emelchenko, *Nanotechnology* 22 (2011).
- [34] S. R. Parnell, A. L. Washington, A. J. Parnell, A. Walsh, R. M. Dalgliesh, F. Li, W. A. Hamilton, S. Prevost, J. P. A. Fairclough, R. Pynn, *Soft Matter* 12 (2016) 4709–14.
- [35] SasView for Small Angle Scattering Analysis, URL: <http://www.sasview.org>.
- [36] N. F. Berk, K. A. Hardman-Rhyne, *J. Appl. Cryst.* 21 (1988) 645–651.
- [37] T. Steiner, W. Saenger, R. E. Lechner, *Mol. Phys.* 72 (1991) 1211–1232.

Appendix A: An effect of wavelength resolution

To estimate an effect of wavelength resolution on measured visibility, let us model the wavelength spread, $p(\lambda)$, by a gaussian with a standard deviation σ_λ and the mean wavelength $\tilde{\lambda}$. Then, for a given pixel coordinate, x :

$$\int p(\lambda) \cos(2\pi x/\zeta) d\lambda = \int p(\lambda) \cos(Cx\lambda) d\lambda = \cos(Cx\tilde{\lambda}) \exp(-(Cx\sigma_\lambda)^2/2) \quad (\text{A.1})$$

where $C = 2c(B_2 - B_1) \cot \theta_0$ (cf. eq. 4). Thus, the reduction of oscillation amplitude is given by

$$R_{\Delta\lambda}(x) = \exp(-(Cx\sigma_\lambda)^2/2) \quad (\text{A.2})$$

and increases towards detector edges, i.e. towards larger $|x|$.

The usable detector width, $-x^{max} < x < x^{max}$, depends on the minimum acceptable $R_{\Delta\lambda}$ -value, $R_{\Delta\lambda}^{min}$. To observe at least one oscillation period, ζ should not exceed $2x^{max}$. Using eq. 10 this constraint can be transformed into a constraint on the minimum observable spin-echo length:

$$\delta_{SE \Delta\lambda}^{min} = \tilde{\lambda} d_1 / (2x^{max}) \quad (\text{A.3})$$

where x^{max} can be calculated from eq. A.2 and $R_{\Delta\lambda}^{min}$.

Specifically, if FWHM of a gaussian is $\Delta_\lambda = \tilde{\lambda} d\lambda/\lambda$, then, $\sigma_\lambda = \Delta_\lambda / (2\sqrt{2 \ln 2})$, leading to

$$x^{max} = 4\sqrt{-\ln(2) \ln(R_{\Delta\lambda}^{min})} / (C\tilde{\lambda}(d\lambda/\lambda)) \quad (\text{A.4})$$

Then, from eqs. A.4 and A.3:

$$\delta_{SE \Delta\lambda}^{min} = \delta_{SE} \frac{\pi(d\lambda/\lambda)}{4\sqrt{-\ln(2) \ln(R_{\Delta\lambda}^{min})}} \quad (\text{A.5})$$

Thus, the constraint $\delta_{SE} \geq \delta_{SE \Delta\lambda}^{min}$ is satisfied when

$$d\lambda/\lambda \leq \frac{4\sqrt{-\ln(2) \ln(R_{\Delta\lambda}^{min})}}{\pi} \quad (\text{A.6})$$

For SKADI, $d\lambda/\lambda$ is expected to be in the range of 4%-8% and will certainly not exceed 20 % [9]. From eq. A.6, for $d\lambda/\lambda = 0.2$, expected $R_{\Delta\lambda}^{min}$ is $0.965 \approx 1$. Thus, for this setup, finite wavelength resolution has no significant impact on the minimum δ_{SE} that can be achieved.

Let us calculate the x coordinate when the decrease in the oscillation amplitude becomes smaller than $R_{\Delta\lambda}$. From eqs. 4, A.2, as well as from C , σ_λ , and Δ_λ defined above:

$$x(R_{\Delta\lambda}, d\lambda/\lambda) = \frac{2\zeta\sqrt{-\ln R_{\Delta\lambda} \ln 2}}{\pi(d\lambda/\lambda)} \quad (\text{A.7})$$

which can be rewritten as

$$R_{\Delta\lambda}(x) = \exp(-(\frac{\pi d\lambda}{2} \frac{x}{\zeta})^2 / \ln 2) \quad (\text{A.8})$$

Appendix B: An effect of the spatial detector resolution on δ_{SE}^{max}

To estimate an effect of the spatial detector resolution on measured visibility, we calculate the average over the width of one detector pixel, p :

$$\frac{1}{p} \int_{\tilde{x}-p/2}^{\tilde{x}+p/2} \cos(\frac{2\pi}{\zeta} x) dx = \cos(\frac{2\pi}{\zeta} \tilde{x}) \frac{\sin(\pi p/\zeta)}{p\pi/\zeta} \quad (\text{B.1})$$

where \tilde{x} is the coordinate of the center of the pixel. The reduction of oscillation amplitude is

$$R_{pixel} = \frac{\sin(\pi p/\zeta)}{p\pi/\zeta} \approx 1 - (p\pi/\zeta)^2/6 \quad (\text{B.2})$$

Once the minimum acceptable R_{pixel} is set, the minimum ζ can be found by numerical solution of eq. B.2 (the approximation in eq. B.2 is not fulfilled when $p\pi/\zeta$ gets large

due to a small ζ). The maximum δ_{SE} due to a finite spatial resolution of SEMSANS detector is

$$\delta_{SE \text{ pixel}}^{max} = \frac{\lambda d_1}{\zeta_{min}} \quad (\text{B.3})$$

$\delta_{SE \text{ pixel}}^{max}$ given in Tab. 1 were calculated for $R_{\text{pixel}}^{min} = 0.75$.

Appendix C: An effect of acceptance angles on the normalized visibility

In the absence of the sample, the intensity of spin-up (+) and spin-down (-) neutrons as a function of detector pixel coordinates x and y is an integral over all possible neutron trajectories:

$$I_{se \ 0}^{\pm}(x, y) = \int ds_x \int ds_y \int d\theta_i \int d\psi_i I_0(s_x, s_y, \theta_i, \psi_i) \times \frac{1 \pm P_0(s_x, s_y, \theta_i, \psi_i) \cos(2\pi x/\zeta)}{2} \quad (\text{C.1})$$

where s_x and s_y are the x - and y -coordinates of a neutron at the sample aperture and θ_i and ψ_i are the incident angles in the XZ and YZ -planes, respectively. This equation is a generalization of eq. 7, but we neglect effects of finite wavelength and detector resolution (cf. eq. 8).

For any given pair of x and s_x , and y and s_y , θ_i and ψ_i are fixed by definition:

$$\theta_i = (x - s_x)/d_1 \quad \psi_i = (y - s_y)/d_1 \quad (\text{C.2})$$

hence, eq. C.1 can be written as

$$I_{se \ 0}^{\pm}(x, y) = I_0^{sum}(x, y)/2 \pm I_0^{mod}(x, y)/2 \quad (\text{C.3})$$

where

$$I_0^{sum}(x, y) = \int ds_x \int ds_y I_0(s_x, s_y, \theta_i, \psi_i) \quad (\text{C.4})$$

$$I_0^{mod}(x, y) = \int ds_x \int ds_y I_0(s_x, s_y, \theta_i, \psi_i) P_0(s_x, s_y, \theta_i, \psi_i) \times \cos\left(\frac{2\pi x}{\zeta}\right) \quad (\text{C.5})$$

The visibility, $V_0(x, y)$, is defined by (cf. eq. 7):

$$V_0(x, y) \cos(2\pi x/\zeta) = I_0^{mod}(x, y)/I_0^{sum}(x, y) \quad (\text{C.6})$$

When a sample is present, the intensity is

$$I_{se}^{\pm}(x, y) = T I_{se \ 0}^{\pm}(x, y) + I^{sum}(x, y)/2 \pm I^{mod}(x, y)/2 \quad (\text{C.7})$$

where the first term describes the contribution from direct beam, T is the sample transmission defined in eq. E.1. Sample scattering comes in via:

$$I^{sum}(x, y) = \int ds_x \int ds_y \int d\theta_i \int d\psi_i S(s_x, s_y, \theta_i, \theta_f, \psi_i, \psi_f) \quad (\text{C.8})$$

and, using $x = s_x + d_1\theta_i$ from eq. C.2:

$$I^{mod}(x, y) = \int ds_x \int ds_y \int d\theta_i \int d\psi_i \cos\left(2\pi \frac{\theta_i d_1 + s_x}{\zeta}\right) \times P_0(s_x, s_y, \theta_i, \psi_i) S(s_x, s_y, \theta_i, \theta_f, \psi_i, \psi_f) \quad (\text{C.9})$$

where θ_f and ψ_f are the angles after scattering,

$S(s_x, s_y, \theta_i, \theta_f, \psi_i, \psi_f)$ is an effective scattering function which includes multiple scattering and sample attenuation and self-absorption, it will be denoted as S_{eff} for brevity. The pixel coordinates x and y are related to the coordinates at the slit via:

$$x = s_x + d_1 \tan \theta_f \approx s_x + d_1 \theta_i + d_1 \theta_s \quad (\text{C.10})$$

$$y = s_y + d_1 \tan \psi_f \approx s_y + d_1 \psi_i + d_1 \psi_s \quad (\text{C.11})$$

where $\theta_s = \theta_f - \theta_i$ and $\psi_s = \psi_f - \psi_i$ are the scattering angles in the XZ and YZ planes, respectively.

From eq. C.11, using $k_0 = 2\pi/\lambda$, $Q_x \approx k_0 \theta_s$, $Q_y \approx k_0 \psi_s$, $d\theta_i = dQ_x/k_0$, $d\psi_i = dQ_y/k_0$, and defining spin-echo length $\delta_{SE} = \lambda d_1/\zeta$, eq. C.8 can be written as

$$I^{sum}(x, y) = \int ds_x \int ds_y \int_0^{Q_x^{max}} dQ_x \int_0^{Q_y^{max}} dQ_y \frac{S_{eff}}{k_0^2} \quad (\text{C.12})$$

where Q_x^{max} is a function of x and s_x , and Q_y^{max} depends on s_y and y . Further

$$I^{mod}(x, y) = \cos\left(\frac{2\pi x}{\zeta}\right) \int ds_x \int ds_y \int_0^{Q_x^{max}} dQ_x \int_0^{Q_y^{max}} dQ_y \cos(Q_x \delta_{SE}) \frac{S_{eff}}{k_0^2} P_0(s_x, s_y, \theta_i, \psi_i) + \sin\left(\frac{2\pi x}{\zeta}\right) \int ds_x \int ds_y \times \int_0^{Q_x^{max}} dQ_x \int_0^{Q_y^{max}} dQ_y \sin(Q_x \delta_{SE}) \frac{S_{eff}}{k_0^2} P_0(s_x, s_y, \theta_i, \psi_i) \quad (\text{C.13})$$

Assuming that S_{eff} is symmetric with respect to Q_x , the second integral in eq. C.13 is zero, which leads to

$$I^{mod}(x, y) = \cos(2\pi \frac{x}{\zeta}) \int ds_x \int ds_y \int_0^{Q_x^{max}} dQ_x \int_0^{Q_y^{max}} dQ_y \cos(Q_x \delta_{SE}) \frac{S_{eff}}{k_0^2} P_0(s_x, s_y, \theta_i, \psi_i) \quad (C.14)$$

The visibility, $V(x, y)$, is defined by

$$V(x, y) \cos(2\pi x/\zeta) = \frac{TI_0^{mod}(x, y) + I^{mod}(x, y)}{TI_0^{sum}(x, y) + I^{sum}(x, y)} \quad (C.15)$$

Normalized visibility is given by:

$$V_s(\delta_{SE}) = \frac{V(x, y)}{V_0(x, y)} = \frac{T + I^{mod}(x, y)/I_0^{mod}(x, y)}{T + I^{sum}(x, y)/I_0^{sum}(x, y)} \quad (C.16)$$

Here, the division by $I_0^{sum}(x, y)$ is a normalization to the incident flux, and the division by $I_0^{mod}(x, y)$ normalizes to the incident flux, and the empty beam polarization.

Thus, the following two functions have to be obtained:

$$\langle I^{sum} \rangle = \frac{I^{sum}(x, y)}{I_0^{sum}(x, y)} = \frac{2\pi}{k_0^2} \int_0^{Q^{max}} S_{eff} Q dQ \quad (C.17)$$

$$\langle I^{mod} \rangle = \frac{I^{mod}(x, y)}{I_0^{mod}(x, y)} = \frac{2\pi}{k_0^2} \int_0^{Q^{max}} J_0(Q \delta_{SE}) S_{eff} Q dQ \quad (C.18)$$

where, for simplicity, we reduced a double integral over Q_x and Q_y to the integral over Q (under assumption of isotropic scattering and that $Q^{max} = Q_x^{max} \approx Q_y^{max}$).

To calculate functions from eqs. C.17, C.18, we use the approach of Schelten and Schmatz and define two functions: $S(Q)$ which is S_{eff} for a very thin sample, and $H(Q)$ which is S_{eff} for an arbitrary thickness t . Eqs. 10-11 from Ref. [18] read

$$s(\delta_{SE}) = 2\pi \int_0^\infty J_0(Q \delta_{SE}) S(Q) Q dQ \quad (C.19)$$

$$h(\delta_{SE}) = 2\pi \int_0^\infty J_0(Q \delta_{SE}) H(Q) Q dQ \quad (C.20)$$

From eq. 12 in Ref. [18]:

$$h(\delta_{SE}) = T k_0^2 [\exp(s(\delta_{SE})/k_0^2) - 1] \quad (C.21)$$

where T is the sample transmission. $H(Q)$ is given by

$$H(Q) = \frac{1}{2\pi} \int_0^\infty J_0(Q \delta_{SE}) h(\delta_{SE}) \delta_{SE} d\delta_{SE} \quad (C.22)$$

We start by noting that $S(Q) = t \frac{d\Sigma(Q)}{d\Omega}$ and calculate $s(\delta_{SE})$ from eq. C.20 as

$$s(\delta_{SE}) = t 2\pi \int_0^\infty J_0(Q \delta_{SE}) \frac{d\Sigma(Q)}{d\Omega} Q dQ = G_{tot}(\delta_{SE}) \xi_{tot} 4\pi^2 t \quad (C.23)$$

Then we calculate $h(\delta_{SE})$ from eq. C.21 and, after that, $S_{eff} = H(Q)$ from eq. C.22. Finally, we calculate $\langle I^{sum} \rangle$ and $\langle I^{mod} \rangle$ from eqs. C.17, C.18 and use them to express $V_s(\delta_{SE})$ from eq. C.16 as:

$$V_s(\delta_{SE}) = \frac{T + \frac{2\pi}{k_0^2} \int_0^{Q^{max}} J_0(Q \delta_{SE}) H(Q) Q dQ}{T + \frac{2\pi}{k_0^2} \int_0^{Q^{max}} H(Q) Q dQ} \quad (C.24)$$

Let us check the limit of eq. C.16 as $Q^{max} \rightarrow \infty$. From eqs. C.17, C.18, and C.20 we arrive at

$$V_s(\delta_{SE}) = \frac{T + h(\delta_{SE})/k_0^2}{T + h(0)/k_0^2} \quad (C.25)$$

and, using eq. C.21 we arrive at

$$V_s(\delta_{SE}) = \exp([s(\delta_{SE}) - s(0)]/k_0^2) \quad (C.26)$$

which is the same as eq. 9, as can be seen from eqs. C.23, and eqs. 14.,15.

Please note that eq. C.24 also applies to the normalized polarisation measured in SESANS experiments.

Note also that the normalized visibility defined by eq. C.16 implicitly depends on x - and y -coordinates. Indeed, $\langle I^{sum} \rangle$ and $\langle I^{mod} \rangle$ from eqs. C.17, C.18 depend on the integration range in Q space, and this range depends on the range of accepted angles, and thus on x and y . However, for the central part of the SEMSANS detector ($x \approx 0$, $y \approx 0$) such dependence is negligible, as can be seen from Appendix D.

Appendix D: The range of accepted scattering angles in SEMSANS

As can be seen from Fig. D.1, the range of incident angles in the XZ plane is limited to $\theta_i = \pm(S_C + S)/d_C$. For the pixel coordinate x , the limits on $\theta_f(x)$ are $(x \pm S)/d_1$. Thus, the limits of $\theta_s(x) = \theta_f(x) - \theta_i$ are

$$\theta_s(x) \in \left(\frac{x - S}{d_1} - \frac{S + S_C}{d_C}; \frac{x + S}{d_1} + \frac{S + S_C}{d_C} \right) \quad (D.1)$$

The range of accepted scattering angles in the YZ plane, i.e. angles ψ_s , is defined analogously.

If measured "spin-up" and "spin-down" intensities, $I_{se}^{\pm}(x, y)$ are summed up across the Y axis of the SEMSANS detector, the range of accepted ψ_s will be broader than the range of $\theta_s(x)$. As a result, the assumption $Q^{max} = Q_x^{max} \approx Q_y^{max}$ that was used to write eqs. C.17-C.18 no longer holds. Consequently, in all equations starting with eqs. C.17-C.18 the integral over $|Q|$ has to be exchanged with a double integral over Q_x and Q_y .

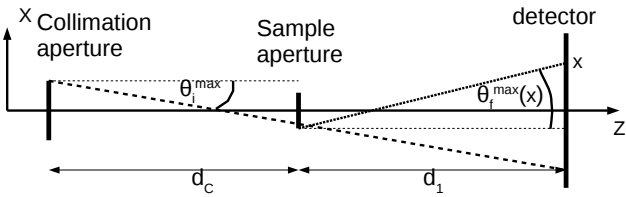


Figure D.1: A sketch of geometrical constraints on incident angles (θ_i) and final angles after scattering (θ_f) for a pixel coordinate x . The sizes of collimation and sample apertures along X axis are $2S_C$ and $2S$, respectively.

Appendix E: Sample transmission and multiple scattering

The fraction of the incident beam that did not interact with a sample is given by the sample transmission:

$$T(\lambda) = \exp(-[\Sigma_a(\lambda) + \Sigma_{coh}(\lambda) + \Sigma_{inc}(\lambda)]t) \quad (\text{E.1})$$

where t is sample thickness; $\Sigma_a(\lambda)$, $\Sigma_{coh}(\lambda)$, and $\Sigma_{inc}(\lambda)$ are macroscopic absorption, coherent and incoherent scattering cross-section, respectively. Σ_{inc} are assumed to be λ -independent and calculated from the atomic and isotopic sample composition using tabulated bound atom cross-sections. $\Sigma_{coh}(\lambda)$ is calculated from

$$\Sigma_{coh}(\lambda) = \int_{4\pi} \frac{d\Sigma(Q)}{d\Omega} d\Omega = \frac{\lambda^2}{2\pi} \int_0^{Q^{max}} \frac{d\Sigma(Q)}{d\Omega} Q dQ \quad (\text{E.2})$$

where $Q = (4\pi/\lambda) \sin \theta/2$ and an isotropic scattering pattern is assumed. In general, $\frac{d\Sigma(Q)}{d\Omega}$ is the coherent differential scattering cross-section, and $Q^{max} = 4\pi/\lambda$. We

neglected wide-angle coherent scattering and calculated $\frac{d\Sigma(Q)}{d\Omega}$ using a SANS model and coherent bound scatter-

For $Q \geq 1 \text{ \AA}^{-1}$, a SANS model can not be expected to be reliable because the approximation of a continuous scattering length density distribution no longer holds. Therefore, Q^{max} is set to $4\pi/\lambda$ when $4\pi/\lambda \leq 1 \text{ \AA}^{-1}$, and 1 \AA^{-1} otherwise.

To estimate the significance of multiple small-angle scattering in the SANS experiment, we use

$$T_{SANS}(\lambda) = \exp(-\Sigma_{SANS}(\lambda)t) \quad (\text{E.3})$$

where $\Sigma_{SANS}(\lambda)$ is calculated from eq. E.2, with Q^{max} set to Q_{SANS}^{max} from eq. 17 and the lower integration limit is set to Q_{SANS}^{min} from eq. 16. Thus, only scattered neutrons that reach the two SANS detectors are taken into account. Then, the significance of multiple scattering is estimated as follows [37].

If the probability to be scattered once is x , twice x^2 etc, then, since $x < 1$, the sum of all scattered neutrons is $x/(1-x)$. At the same time, it is just $1 - T_{SANS}$. The result is $x = \frac{1-T_{SANS}}{2-T_{SANS}}$ and the fraction of multiply scattered neutrons to all scattered neutrons is $M = ([x/(1-x)]-x)/[x/(1-x)] = x$. For example, for $T_{SANS} = 90\%$, M is 9%, for $T_{SANS} = 80\%$, M is 17%. Please note that this is only a rough estimate and that multiple small angle scattering will also be attenuated by absorption and incoherent scattering.